



Control of single-ligand chemistry on thiolated Au₂₅ nanoclusters

Yitao Cao¹, Victor Fung ², Qiaofeng Yao ¹, Tiankai Chen¹, Shuangquan Zang ³, De-en Jiang ²✉ & Jianping Xie ^{1,4}✉

Diverse methods have been developed to tailor the number of metal atoms in metal nanoclusters, but control of surface ligand number at a given cluster size is rare. Here we demonstrate that reversible addition and elimination of a single surface thiolate ligand (-SR) on gold nanoclusters can be realized, opening the door to precision ligand engineering on atomically precise nanoclusters. We find that oxidative etching of [Au₂₅SR₁₈]⁻ nanoclusters adds an excess thiolate ligand and generates a new species, [Au₂₅SR₁₉]⁰. The addition reaction can be reversed by CO reduction of [Au₂₅SR₁₉]⁰, leading back to [Au₂₅SR₁₈]⁻ and eliminating precisely one surface ligand. Intriguingly, we show that the ligand shell of Au₂₅ nanoclusters becomes more fragile and rigid after ligand addition. This reversible addition/elimination reaction of a single surface ligand on gold nanoclusters shows potential to precisely control the number of surface ligands and to explore new ligand space at each nuclearity.

¹Department of Chemical and Biomolecular Engineering, National University of Singapore, 4 Engineering Drive 4, Singapore 117585, Singapore. ²Department of Chemistry, University of California, Riverside, CA 92521, USA. ³Green Catalysis Center, and College of Chemistry, Zhengzhou University, 450001 Zhengzhou, China. ⁴Joint School of National University of Singapore and Tianjin University, International Campus of Tianjin University Binhai New City, 350207 Fuzhou, China. ✉email: djiang@ucr.edu; chexiej@nus.edu.sg

Metal nanoclusters have received tremendous research interests in the past two decades due to their atomically-precise structures, intriguing physicochemical properties, and wide potential applications^{1–5}. Because of the atomically-precise nature of metal nanoclusters, delicate control of cluster size in synthesis has long been the crucial prerequisite in research^{1–6}. Taking thiolate-protected Au nanoclusters as an example, the most traditional and widely-used method is the chemical reduction of Au(I)-thiolate precursors followed by a size-focusing process^{7,8}. It has been reported that, in the size-focusing process, oxygen (O₂)-generated thiol radicals can induce the selective etching of metastable intermediates by drawing out Au atoms from the metallic core (i.e., top-down process)⁹. As a result, the polydisperse species will transform to thermodynamically stable monodisperse final products.

Thiolate-protected metal nanoclusters are often referred to as [M_nSR_m]^q (SR denotes thiolate ligands), where *n*, *m*, *q* represent numbers of metal atoms, thiolate ligands and net charge, respectively. The size-focusing will change the *n* value and result in some thermodynamically stable magic sizes, such as [Au₂₅SR₁₈][−]. The high stability of [Au₂₅SR₁₈][−] can be explained by the valence electron counts (*N*^{*} = *n* − *m* − *q*) of 8, which fulfills the shell closing phenomenon¹⁰. As a result, [Au₂₅SR₁₈][−] is one of the typical species survived in the size-focusing or ligand-induced etching process^{11,12}. Its oxidation will simply change the *q* value from −1 to 0 or +1 and introduce slight distortion into its structure, without changing the total molecular formula^{13–15}.

Tailoring of surface ligands is equally important considering the total synthesis of metal nanoclusters⁶. The surface ligands will greatly influence the cluster size, as well as physicochemical properties, self-assembly behavior, stability and so on^{16–27}. Ligand exchange reaction is the main technique used to tailor the surface ligands of thiolate-protected metal nanoclusters²⁸. One possible result of a ligand exchange reaction is partial or total substitution of surface ligands without altering the total formula of the parent cluster^{29,30}. The other one is the complete change of cluster size, the so-called ligand-exchange-induced size/structure transformation process, which has been applied to discover new cluster species^{16,31}. However, all the above methodologies have not addressed an important challenge to precisely control the number of surface ligands (*m* value) by adding/removing a single ligand at a time for a given number of metal atoms (*n* value).

To meet the challenge, here we successfully realized the addition and elimination of a surface ligand in thiolate-protected gold nanoclusters based on [Au₂₅SR₁₈][−], the flagship cluster of the [M_nSR_m]^q family. We demonstrated the reversible conversion between water-soluble [Au₂₅SR₁₈][−] and [Au₂₅SR₁₉]⁰ nanoclusters with identical thiolate ligand through an oxidative etching/reduction cycle (Fig. 1). Detailed evidence from electrospray ionization mass spectrometry (ESI-MS) indicated a continuous oxidation process of the as-prepared [Au₂₅SR₁₈][−] (*N*^{*} = 8) to [Au₂₅SR₁₈]⁰ (*N*^{*} = 7), and then to [Au₂₅SR₁₈]⁺ (*N*^{*} = 6). [Au₂₅SR₁₈]⁺ nanoclusters then reacted with an excess thiolate ligand to form a new isoelectric species, [Au₂₅SR₁₉]⁰ (*N*^{*} = 6),

realizing the addition of one thiolate ligand to the original nanocluster. The reverse process can be realized by carbon monoxide (CO)-reduction reaction to eliminate one thiolate ligand in [Au₂₅SR₁₉]⁰ and regenerate [Au₂₅SR₁₈][−].

Results

Synthesis of Au nanoclusters. [Au₂₅(MHA)₁₈][−] (MHA = 6-mercaptopentanoic acid) was selected as the model cluster in the oxidative etching exploration. The as-prepared sample clearly shows characteristic absorption peaks of [Au₂₅SR₁₈][−] (Fig. 2a, 400, 440, 543, 675, and 800 nm)³². Electrospray ionization mass spectrometry (ESI-MS) also indicates the successful synthesis of [Au₂₅(MHA)₁₈][−] species (Fig. 2c). Note that purification was needed before ESI-MS tests, during which the partial oxidation of [Au₂₅(MHA)₁₈][−] already took place. As a result, the species captured in ESI-MS were from a mixture of [Au₂₅(MHA)₁₈][−] and [Au₂₅(MHA)₁₈]⁰.

Oxidative etching exploration and product identification. The as-prepared [Au₂₅(MHA)₁₈][−] nanoclusters were then dialyzed (with a dialysis membrane of molecular weight cut-off of 5000 Da) and the pH was lowered to 9.0 ± 0.2 to accelerate the oxidation (see Supplementary Fig. 1). The characteristic absorption peaks of [Au₂₅MHA₁₈][−] disappeared completely within 24 h. Polyacrylamide gel electrophoresis (PAGE) was applied to analyze and purify the final product (Supplementary Fig. 2). The main product was separated for further characterization. UV-Vis absorption spectrum shows significantly blue-shifted absorption band edge compared to [Au₂₅MHA₁₈][−] and characteristic absorption peaks at 440, 545, and 585 nm (Fig. 2b), indicating the formation of a new species. ESI-MS was then applied to determine its molecular formula (Fig. 2d). The isotope pattern only matched well with [Au₂₅MHA₁₉]⁰, a species with the same nuclearity but different ligand number. Thus, it seems possible to precisely adding one thiolate ligand into [Au₂₅MHA₁₈][−].

Mechanism of the ligand addition reaction. To further verify this addition reaction and examine its mechanism, we simplified the whole reaction system by removing the excess ligands, Au(I)-complexes and inorganic ions remained in the solution using PAGE separation. These species may cause the side reactions and the formation of by-products, and a typical dialysis may not be able to completely remove them. The absorption spectrum of the purified [Au₂₅MHA₁₈][−] species was shown in Fig. 3a.

ESI-MS was then applied to monitor the variation of [Au₂₅MHA₁₈][−] species after the long-time exposure in air. The overall spectrum indicates the high purity of [Au₂₅MHA₁₈][−] species (Fig. 3b). However, in a detailed analysis of isotopic patterns (Fig. 3c), we found that the majority of [Au₂₅MHA₁₈][−] species have been oxidized from [Au₂₅MHA₁₈][−] (*N*^{*} = 8) to [Au₂₅MHA₁₈]⁰ (*N*^{*} = 7). Furthermore, we noticed an excess small peak that can only be assigned to [Au₂₅MHA₁₈]⁺ (*N*^{*} = 6), product originated from the further oxidation of [Au₂₅MHA₁₈][−] species. Actually, it is the first time that the water-soluble [Au₂₅SR₁₈][−] was found to be oxidized to the valence state of +1¹³. As no external oxidant was added to the solution to induce the reaction, the only oxidation resource in this reaction should be O₂ in the air. The signals shown in Fig. 3d further support this conjecture. We clearly observed the signals which could be assigned to [Au₂₅MHA₁₈]^{δ+} + O^{δ−} adducts. This assignment was supported by the fact that these signals become stronger after introducing excess oxidation reagent such as H₂O₂ (Supplementary Fig. 3). The [Au₂₅MHA₁₈]^{δ+} + O^{δ−} adducts should be the intermediate in the reaction between molecular O₂ and [Au₂₅MHA₁₈][−] nanoclusters to generate [Au₂₅MHA₁₈]⁺.

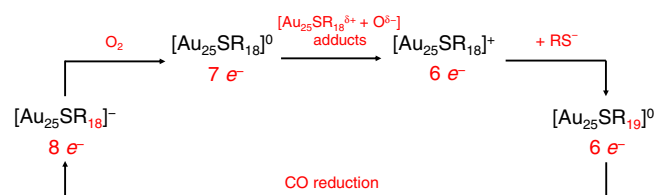


Fig. 1 Schematic illustration of reaction process. Schematic illustration of the addition/elimination reaction cycle between [Au₂₅SR₁₈][−] and [Au₂₅SR₁₉]⁰.

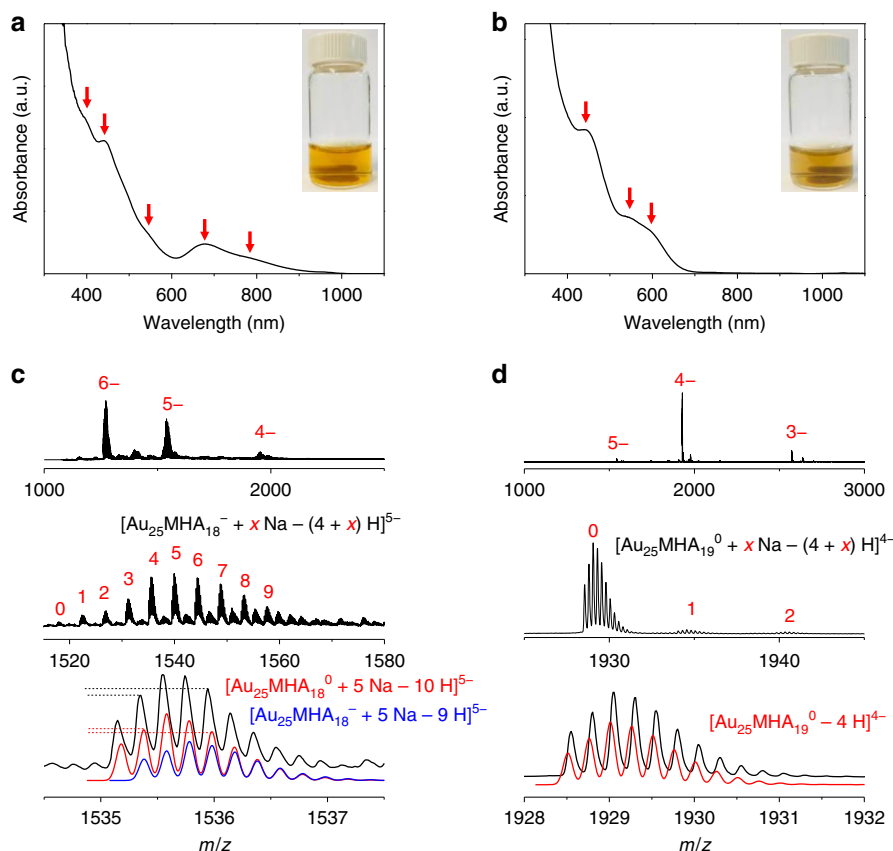


Fig. 2 Characterization of the Au₂₅ species. UV-Vis absorption spectra of as-prepared (a) [Au₂₅MHA₁₈]⁻ and (b) [Au₂₅MHA₁₉]⁰. Insets show the digital images of the solution of corresponding species. Red arrows indicate the positions of characteristic absorption peaks. ESI-MS spectra of (c) [Au₂₅MHA₁₈]⁻ and (d) [Au₂₅MHA₁₉]⁰. Both experimental and simulated spectra are shown. Dash lines in c are guidelines to judge the relative intensity of corresponding isotopic peaks. The discrepancy between the experimental and simulated result indicate the co-existence of [Au₂₅MHA₁₈]⁻ and [Au₂₅MHA₁₈]⁰.

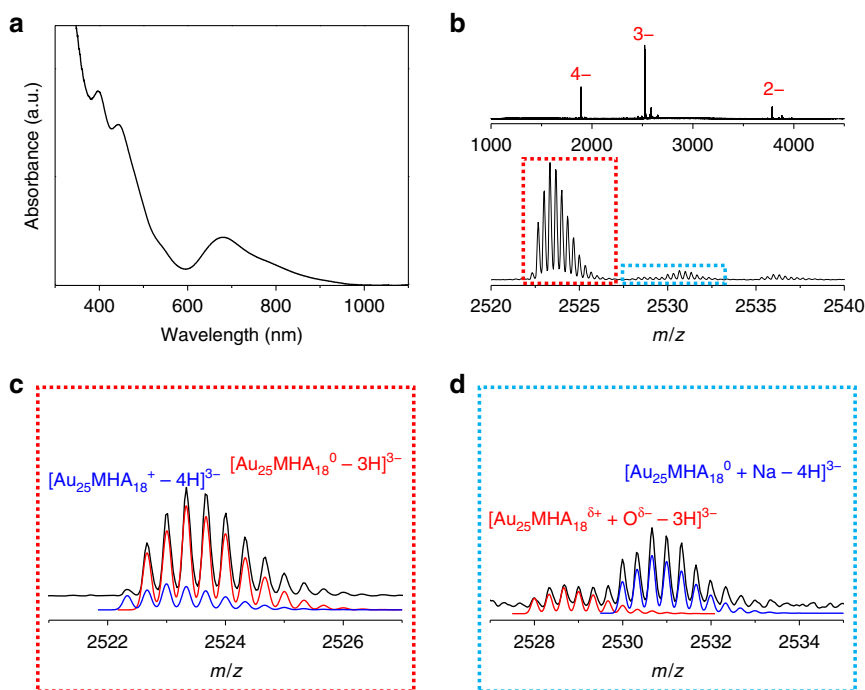


Fig. 3 Monitoring of reaction intermediates. a UV-Vis absorption and b ESI-MS spectra of [Au₂₅MHA₁₈] species after PAGE purification and long-time exposure in air. Detailed analysis of the enlarged parts in red and blue square is shown in c and d, respectively. Both experimental and simulated isotopic patterns of labeled species are included.

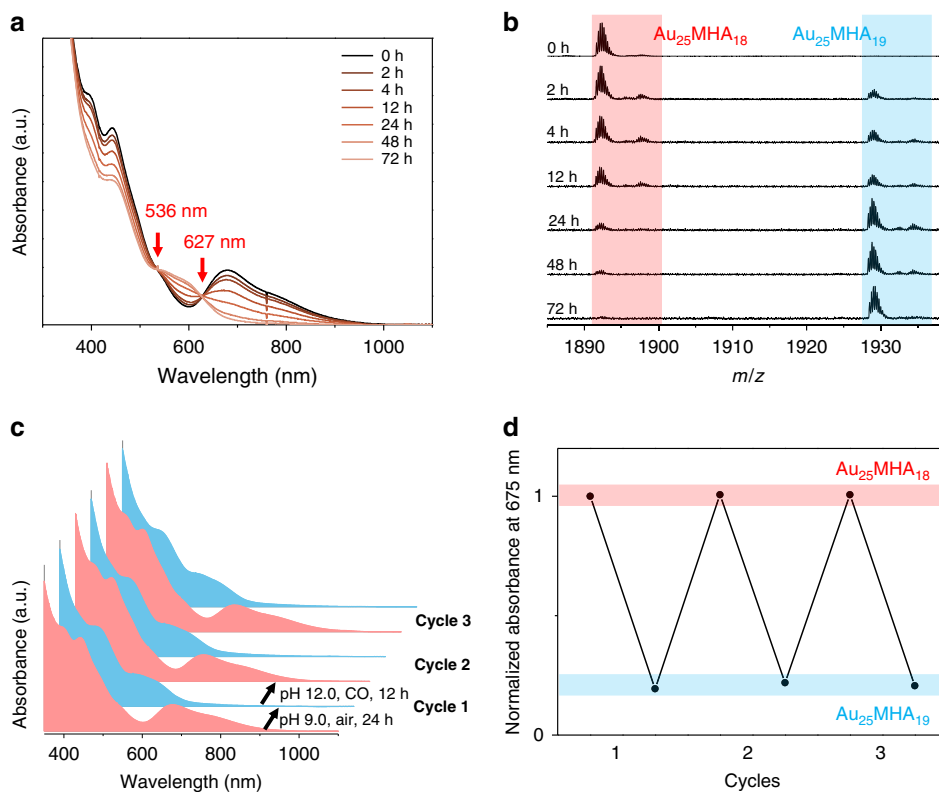


Fig. 4 Interconversion process. **a** Time-course UV-Vis absorption spectra and **b** ESI-MS spectra in the transformation from $[\text{Au}_{25}\text{MHA}_{18}]$ species to $[\text{Au}_{25}\text{MHA}_{19}]^0$ after introducing excess thiol ligands. **c** and **d** show the oxidative etching/reduction cycles between $[\text{Au}_{25}\text{MHA}_{18}]^-$ and $[\text{Au}_{25}\text{MHA}_{19}]^0$ by UV-vis absorption spectra and normalized absorbance at 675 nm in the reversible transformation process, respectively.

Further prolonging the oxidation reaction time will not increase the abundance of $[\text{Au}_{25}\text{MHA}_{18}]^+$ (Supplementary Fig. 4a), indicating an equilibrium between $[\text{Au}_{25}\text{MHA}_{18}]^0$ and $[\text{Au}_{25}\text{MHA}_{18}]^+$ species. However, introducing reducing reagent such as CO and oxidation reagent such as H_2O_2 will suppress and increase the signals corresponding to $[\text{Au}_{25}\text{MHA}_{18}]^+$, respectively, further confirming our assignments (Supplementary Fig. 4b and 4c). Since $[\text{Au}_{25}\text{MHA}_{18}]^+$ and final product $[\text{Au}_{25}\text{MHA}_{19}]^0$ have the same N^* value of 6, oxidation is not needed in subsequent transformation process. At this stage, $[\text{Au}_{25}\text{MHA}_{18}]^+$ reacting with one free thiol ligand will drive the isoelectric reaction to the final product $[\text{Au}_{25}\text{MHA}_{19}]^0$.

Reversible conversion process. We thus introduced excess thiol ligands into the solution and monitor the transformation process by UV-vis absorption spectroscopy and real-time ESI-MS. We observed two isosbestic points in the UV-vis absorption spectra at 536 and 627 nm (Fig. 4a), which indicates a quasi-one-to-one transformation process (Supplementary Note 1). The ESI-MS spectra (Fig. 4b) also showed a gradual consuming of $[\text{Au}_{25}\text{MHA}_{18}]$ species and generating of $[\text{Au}_{25}\text{MHA}_{19}]^0$ without other observable intermediates. The final product was shown to be pure $[\text{Au}_{25}\text{MHA}_{19}]^0$ nanoclusters (Supplementary Fig. 5). Thus, we have successfully demonstrated that one thiolate ligand can be precisely added to one $[\text{Au}_{25}\text{MHA}_{18}]^-$ to form a $[\text{Au}_{25}\text{MHA}_{19}]^0$.

As many chemical reactions are reversible in nature, we then investigated the possibilities to precisely eliminate one ligand from $[\text{Au}_{25}\text{MHA}_{19}]^0$ to $[\text{Au}_{25}\text{MHA}_{18}]^-$. We were able to realize this transformation by introducing a reducing agent, CO, to $[\text{Au}_{25}\text{MHA}_{19}]^0$ solution. Pure $[\text{Au}_{25}\text{MHA}_{18}]^-$ was formed as indicated by UV-Vis absorption and ESI-MS spectra (Supplementary Fig. 6). Furthermore, the oxidative etching of

$[\text{Au}_{25}\text{MHA}_{18}]^-$ and reduction of $[\text{Au}_{25}\text{MHA}_{19}]^0$ can be reversibly realized (Fig. 4c, d) by simply tailoring the pH of the solution and atmosphere (pH ~ 9 , air for oxidative etching and pH ~ 12 , CO for reduction).

Discussion

Change of ligand number on the same nuclearity will inevitably influence the structure of ligand shell and thus the properties of whole nanocluster. We try to gain further insights into differences of the ligand shell after addition/elimination of one excess thiolate ligand using tandem mass spectrometry and nuclear magnetic resonance (NMR) analysis. Tandem mass spectrometry has been widely applied in structural analysis of molecular-like clusters and shows sensitivity in analyzing the surface motifs^{33,34}. As shown in Fig. 5a, b, the onset energy of fragmentation decreased dramatically from 20 eV of $[\text{Au}_{25}\text{MHA}_{18}]$ species (dominant species: $[\text{Au}_{25}\text{MHA}_{18}]^0$) to 5 eV of $[\text{Au}_{25}\text{MHA}_{19}]^0$, indicating a more fragile nature of the surface structure after addition of one excess thiolate ligand. However, these two species showed a similar fragment pattern that the major fragmentation routes are the same by dissociation of one Au_4SR_4 unit stepwise in 1st and 2nd generation fragmentation. In addition, a less prominent 1st generation fragment of $[\text{Au}_{25}\text{MHA}_{19}]^0$ by dissociation of one Au_5SR_5 unit has been detected, which should be the result of lengthened motif after ligand addition.

¹H-NMR signals of surface protecting ligands also provide substantial information of ligand shell in metal nanoclusters^{35–37}. As shown in Fig. 6, the signals of protons in MHA surface ligands can be well assigned into two sets in $[\text{Au}_{25}\text{MHA}_{18}]^-$ (see Supplementary Fig. 9 for assignments of the two kinds of surface ligands). Note that NaBH_4 was introduced to reduce the $[\text{Au}_{25}\text{MHA}_{18}]$ species to -1 state to get a more analyzable spectrum. In the spectrum of $[\text{Au}_{25}\text{MHA}_{19}]^0$, the most obvious

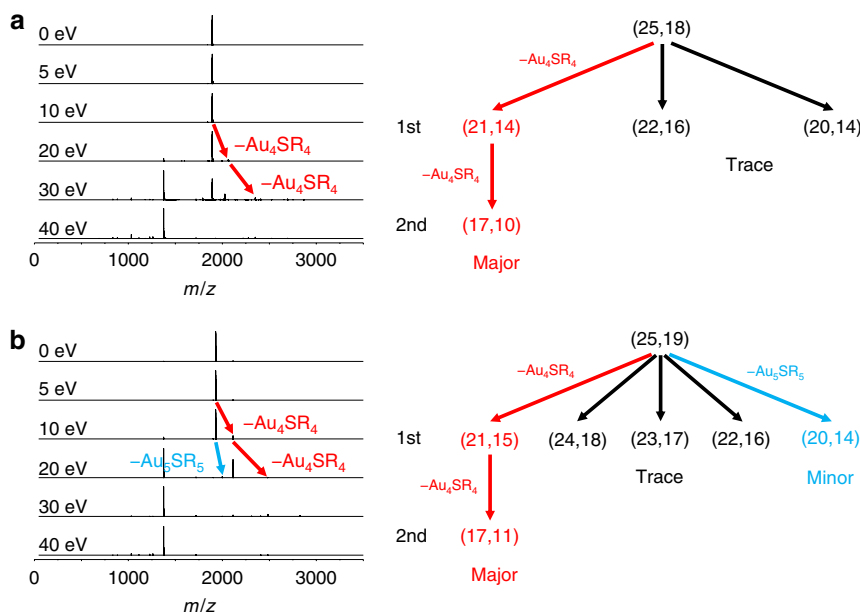


Fig. 5 Tandem mass testing of the Au₂₅ species. Tandem mass spectra and corresponding fragmentation patterns of (a) [Au₂₅MHA₁₈]⁰ and (b) [Au₂₅MHA₁₉]⁰. (*m*, *n*) denotes species with molecular formula of Au_{*m*}SR_{*n*}. Different routes are divided into major, minor, and trace categories based on the abundance in tandem mass spectra. See Supplementary Fig. 7 and 8 for detailed assignments of fragment species.

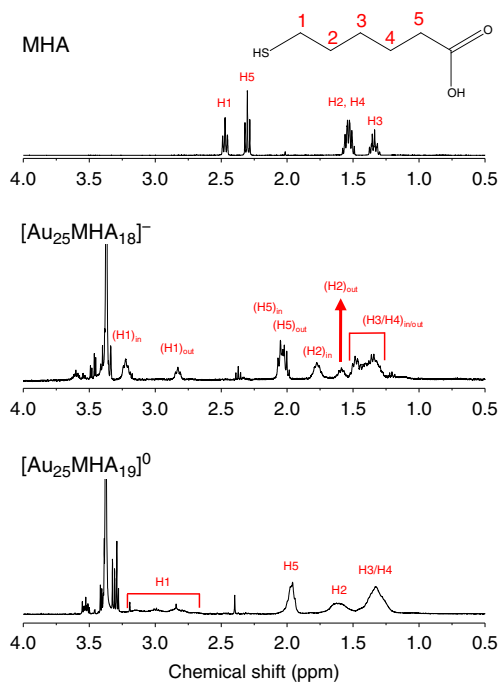
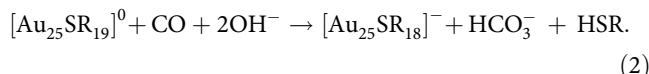
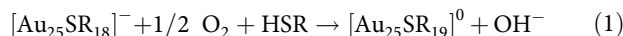


Fig. 6 ¹H-NMR testing of the ligand shell. ¹H-NMR spectra of MHA ligand, [Au₂₅MHA₁₈]⁻, and [Au₂₅MHA₁₉]⁰. Sharp peaks around chemical shift of 3.30 and 2.40 ppm are from impurities introduced in PAGE and ultrafiltration process which are hard to be removed and assigned.

differences of the signals were the largely broadened and smoothed peaks. The broadened and featureless signals were the direct result of limited motion of surface ligands³⁸, indicating a more rigidified ligand shell after addition of one excess thiolate ligand. Note that the peak broadening can also be the result of a distribution of isotropic chemical shift (typically observed in larger metal nanoparticles)³⁹, a paramagnetic core (observed in metal nanoclusters with odd *N*^{*} together with huge down-shift of NMR signals) and electron transfer between different oxidation

states of metal nanoclusters⁴⁰, which are not expected to exist in [Au₂₅MHA₁₉]⁰.

Summing up the experimental evidence above, we think that the single-ligand chemistry and the interconversion of [Au₂₅SR₁₈]⁻ and [Au₂₅SR₁₉]⁰ can be described by the following two reactions:



Energetics for the two reactions can be computed by density functional theory (DFT) and help understand the thermodynamic driving force of the two reactions. To this end, a structural model for [Au₂₅SR₁₉]⁰ would be needed. Given the similar patterns in tandem mass spectra of [Au₂₅SR₁₈]⁻ and [Au₂₅SR₁₉]⁰, we hypothesize that they have a similar ligand shell composition. Indeed, we found that the structural model with a defective icosahedral core and lengthened Au₃SR₄ motif is more stable than many other isomers that we tested (Supplementary Fig. 10; see Supplementary information for computational details). We therefore used this model as our putative structure for [Au₂₅SR₁₉]⁰ when computing the reaction energetics. (Here we note that a total structure prediction for [Au₂₅SR₁₉]⁰ is still computationally demanding and beyond the scope of this work). The computed ΔE at the B3LYP/TZVP level with an implicit solvation model is -0.11 eV for reaction (1) and -4.57 eV for reaction (2), in qualitative agreement with our experimental observation. In other words, when pH is lowered, a single thiol (HSR) ligand can be oxidatively added to [Au₂₅SR₁₈]⁻ under O₂ with a favorable energy gain, while [Au₂₅SR₁₉]⁰ can be reduced back to [Au₂₅SR₁₈]⁻ by CO at higher pH at more favorable energetics.

Besides the favorable energetic of the transformation from [Au₂₅SR₁₈]⁻ to [Au₂₅SR₁₉]⁰ under the oxidative environment in the presence of free thiol ligands, [Au₂₅MHA₁₉]⁰ also shows higher resistance to oxidative etching than [Au₂₅MHA₁₈]⁻ (Supplementary Fig. 11). The enhanced stability of [Au₂₅MHA₁₉]⁰ under the oxidative environment is probably due to the lengthened motifs and rigidified ligand shell, which will provide better

protection to the Au(0) core and prevent the access of oxidative species (e.g., O₂ and thiol radicals). Thus, we were able to obtain the pure product of [Au₂₅MHA₁₉]⁰ by the as-specified oxidative etching reaction.

In conclusion, we successfully demonstrated a reaction cycle composed of precise addition and elimination of one thiolate surface ligand on gold nanoclusters. The addition of one thiolate ligand into the original [Au₂₅MHA₁₈]⁻ nanoclusters was realized by an oxidative etching reaction. In this process, [Au₂₅MHA₁₈]⁻ was first oxidized by O₂ stepwise from -1 state to 0 and +1 state. The [Au₂₅MHA₁₈]⁺ then reacted with one free thiol ligand to generate [Au₂₅MHA₁₉]⁰. Tandem mass spectrometry and ¹H-NMR indicated that addition of one excess ligand resulted in a ligand shell with similar composition, but more fragile and rigid. We further realized the reverse process by CO-reduction, eliminating one thiolate surface ligand and regenerating [Au₂₅MHA₁₈]⁻ nanoclusters. Computed reaction energetics from DFT confirms the driving force of the ligand chemistry and the interconversion of [Au₂₅MHA₁₈]⁻ and [Au₂₅MHA₁₉]⁰. The key point of such manipulation should be using a stoichiometric amount of ligands in the oxidative etching reaction, which creates a mild reaction condition to possibly stabilize the metastable products. This method provides more opportunities in discovery of 'hidden' species at a given nanocluster size (or metal atom number) with precisely controlled surface ligand number and surface rigidity, and generating new physical and chemical properties, such as photoluminescence and catalysis.

Methods

Materials. 6-mercaptohexanoic acid (MHA), were purchased from Sigma-Aldrich. Hydrogen tetrachloroaurate(III) hydrate (HAuCl₄·3H₂O) was purchased from Alfa Aesar. Sodium hydroxide (NaOH) was purchased from Sigma-Aldrich. Carbon monoxide (CO, 99.9%) was obtained from Singapore Oxygen Air Liquide Pte Ltd (SOXAL). All chemicals were used without further purification. Ultrapure water (18.2 MΩ cm) was used in all the experiments. All glassware was washed with aqua regia before use.

Synthesis of [Au₂₅(MHA)₁₈]⁻ nanoclusters. [Au₂₅(MHA)₁₈]⁻ nanoclusters were synthesized through a CO-reduction method. In a typical synthesis, 4 mL of aqueous solution of 5 mM MHA and 0.2 mL of aqueous solution of 50 mM HAuCl₄ were added into 5.8 mL of ultrapure water. After 5 min, the pH of the solution was brought up to 12.0 by dropwise adding aqueous solution of 1 M NaOH. After 30 min, CO was bubbled into the solution for 2 min. The reaction vessel was then kept airtight and the reaction was allowed to proceed for 24 h under gentle stirring (500 rpm) at room temperature. The raw product was either purified by ultrafiltration (membrane of molecular weight cut-off = 5000 Da) before testing electrospray ionization mass spectrometry (ESI-MS), or purified by dialysis (membrane of molecular weight cut-off = 5000 Da) before further oxidation reaction.

Native polyacrylamide gel electrophoresis (PAGE) separation of the Au nanoclusters. In the native PAGE experiments, Bio-Rad Mini-PROTEAN® Tetra Cell or PROTEAN® II xi Cell system was used. Stacking and resolving gels were prepared by 4 and 30 wt% acrylamide monomers (1:19), respectively. The Au nanocluster solutions were first concentrated by ultrafiltration and then mixed with glycerol to prepare the sample solutions (~10 mM based on Au atoms, 50 vol% glycerol). 2 mL of sample solution were loaded into the well. The PAGE was conducted with constant voltage of 180 V for 24 h at 4 °C. The bands were cut, crushed, and incubated in ultrapure water to obtain solutions of pure Au nanoclusters for further use. The cluster concentration was determined by inductively coupled plasma mass spectrometry (ICP-MS) measurements.

Conversion from purified [Au₂₅(MHA)₁₈]⁻ species to [Au₂₅(MHA)₁₉]⁰. Purified [Au₂₅(MHA)₁₈]⁻ species from PAGE were used. In a typical reaction, 1 equivalent excess MHA (40 μM) was introduced into the solution of [Au₂₅(MHA)₁₈]⁻ (~1 mM of [Au]). The solution pH was adjusted to 9.0 ± 0.2. Time-course absorption spectra and ESI-MS spectra were then recorded. Note that the reaction was conducted without stirring in time-course monitoring, and will be accelerated if stirring was applied (completed within 24 h).

Conversion from [Au₂₅(MHA)₁₉]⁰ to [Au₂₅(MHA)₁₈]⁻ by CO reduction. The solution pH was brought up to 12.0 by an aqueous solution of 1 M NaOH. CO was bubbled into the solution for 2 min. The reaction was proceeded for 12 h airtight. The sample needs to be purified by ultrafiltration before ESI-MS test.

Characterizations. Solution pH was recorded by Mettler-Toledo FE 20 pH-meter. UV-vis absorption spectra were recorded by Shimadzu UV-1800 spectrometer. ESI-MS spectra were captured by a Bruker microTOF-Q system in negative ion mode. ESI-MS testing parameters: source temperature 120 °C, dry gas flow rate 8 L per min, nebulizer pressure 3 bar, capillary voltage 3.5 kV, and sample injection rate 3 μL per min. In ESI-MS test, the solution was directly injected without further purification unless specified. ¹H-NMR spectra were recorded on Bruker 400 MHz system using D₂O as solvent. Purified samples were obtained from PAGE separation and further ultrafiltration process.

Data availability

All relevant data are available from the corresponding authors on request.

Received: 25 March 2020; Accepted: 1 October 2020;

Published online: 30 October 2020

References

- Jin, R. C. Atomically precise metal nanoclusters: stable sizes and optical properties. *Nanoscale* **7**, 1549 (2015).
- Jin, R. C., Zeng, C. J., Zhou, M. & Chen, Y. X. Atomically precise colloidal metal nanoclusters and nanoparticles: fundamentals and opportunities. *Chem. Rev.* **116**, 10346 (2016).
- Chakraborty, I. & Pradeep, T. Atomically precise clusters of noble metals: emerging link between atoms and nanoparticles. *Chem. Rev.* **117**, 8208 (2017).
- Kurashige, W., Niihori, Y., Sharma, S. & Negishi, Y. Precise synthesis, functionalization and application of thiolate-protected gold clusters. *Coord. Chem. Rev.* **320**, 238 (2016).
- Yao, Q. F., Yuan, X., Chen, T. K., Leong, D. T. & Xie, J. P. Engineering functional metal materials at the atomic level. *Adv. Mater.* **30**, 1802751 (2018).
- Yao, Q. F., Chen, T. K., Yuan, X. & Xie, J. P. Toward total synthesis of thiolate-protected metal nanoclusters. *Acc. Chem. Res.* **51**, 1338 (2018).
- Brust, M., Walker, M., Bethell, D., Schiffrin, D. J. & Whyman, R. Synthesis of thiol-derivatized gold nanoparticles in a 2-phase liquid-liquid system. *J. Chem. Soc. Chem. Commun.* **0**, 801 (1994).
- Luo, Z. T. et al. Toward understanding the growth mechanism: tracing all stable intermediate species from reduction of Au(I)-thiolate complexes to evolution of Au₂₅ nanoclusters. *J. Am. Chem. Soc.* **136**, 10577 (2014).
- Dreier, T. A. & Ackerson, C. J. Radicals are required for thiol etching of gold particles. *Angew. Chem. Int. Ed.* **54**, 9249 (2015).
- Walter, M. et al. A unified view of ligand-protected gold clusters as superatom complexes. *Proc. Natl Acad. Sci. USA* **105**, 9157 (2008).
- Zhu, M., Lanni, E., Garg, N., Bier, M. E. & Jin, R. Kinetically controlled, high-yield synthesis of Au₂₅ clusters. *J. Am. Chem. Soc.* **130**, 1138 (2008).
- Shichibu, Y. et al. Extremely high stability of glutathionate-protected Au₂₅ clusters against core etching. *Small* **3**, 835 (2007).
- Negishi, Y., Chaki, N. K., Shichibu, Y., Whetten, R. L. & Tsukuda, T. Origin of magic stability of thiolated gold clusters: a case study on Au₂₅(SC₆H₁₃)₁₈. *J. Am. Chem. Soc.* **129**, 11322 (2007).
- Zhu, M. Z., Eckenhoff, W. T., Pintauer, T. & Jin, R. C. Conversion of anionic Au₂₅(SCH₂CH₂Ph)₁₈⁻ cluster to charge neutral cluster via air oxidation. *J. Phys. Chem. C* **112**, 14221 (2008).
- Tofaneli, M. A. et al. Jahn-Teller effects in Au₂₅(SR)₁₈. *Chem. Sci.* **7**, 1882 (2016).
- Zeng, C. J., Chen, Y. X., Das, A. & Jin, R. C. Transformation chemistry of gold nanoclusters: from one stable size to another. *J. Phys. Chem. Lett.* **6**, 2976 (2015).
- Shen, H. et al. Highly robust but surface-active: an N-heterocyclic carbene-stabilized Au₂₅ nanocluster. *Angew. Chem. Int. Ed.* **58**, 17731 (2019).
- Deng, G. C. et al. From symmetry breaking to unraveling the origin of the chirality of ligated Au₁₃Cu₂ nanoclusters. *Angew. Chem. Int. Ed.* **57**, 3421 (2018).
- Chai, J. S. et al. Exposing the delocalized Cu-S π bonds on the Au₂₄Cu₆(SPhtBu)₂₂ nanocluster and its application in ring-opening reactions. *Angew. Chem. Int. Ed.* **58**, 15671 (2019).
- Gan, Z. B. et al. The fourth crystallographic closest packing unveiled in the gold nanocluster crystal. *Nat. Commun.* **8**, 14739 (2017).
- Yuan, S. F., Guan, Z. J., Liu, W. D. & Wang, Q. M. Solvent-triggered reversible interconversion of all-nitrogen-donor-protected silver nanoclusters and their responsive optical properties. *Nat. Commun.* **10**, 4032 (2019).
- Nieto-Ortega, B. & Burgi, T. Vibrational properties of thiolate-protected gold nanoclusters. *Acc. Chem. Res.* **51**, 2811 (2018).
- Huang, R. W. et al. Hypersensitive dual-function luminescence switching of a silver-chalcogenolate cluster-based metal-organic framework. *Nat. Chem.* **9**, 689 (2017).

24. Shichibu, Y. et al. Photoluminescence properties of [core+exo]-type Au₆ clusters: insights into the effect of ligand environments on the excitation dynamics. *J. Phys. Chem. C*, **123**, 6934 (2019).
25. Chevrier, D. M. et al. Molecular-scale ligand effects in small gold-thiolate nanoclusters. *J. Am. Chem. Soc.* **140**, 15430 (2018).
26. Yao, Q. F. et al. Counterion-assisted shaping of nanocluster supracrystals. *Angew. Chem. Int. Ed.* **54**, 184 (2015).
27. Yoon, B. et al. Hydrogen-bonded structure and mechanical chiral response of a silver nanoparticle superlattice. *Nat. Mater.* **13**, 807 (2014).
28. Heinecke, C. L. et al. Structural and theoretical basis for ligand exchange on thiolate monolayer protected gold nanoclusters. *J. Am. Chem. Soc.* **134**, 13316 (2012).
29. Tracy, J. B. et al. Electrospray ionization mass spectrometry of uniform and mixed monolayer nanoparticles: Au₂₅[S(CH₂)₂Ph]₁₈ and Au₂₅[S(CH₂)₂Ph]_(18-x)(SR)_x. *J. Am. Chem. Soc.* **129**, 16209 (2007).
30. Ni, T. W., Tofanelli, M. A., Phillips, B. D. & Ackerson, C. J. Structural basis for ligand exchange on Au₂₅(SR)₁₈. *Inorg. Chem.* **53**, 6500 (2014).
31. Zeng, C. J. et al. Total Structure and electronic properties of the gold nanocrystal Au₃₆(SR)₂₄. *Angew. Chem. Int. Ed.* **51**, 13114 (2012).
32. Yuan, X. et al. Balancing the rate of cluster growth and etching for gram-scale synthesis of thiolate-protected Au₂₅ nanoclusters with atomic precision. *Angew. Chem. Int. Ed.* **53**, 4623 (2014).
33. Yao, Q. F. et al. Precise control of alloying sites of bimetallic nanoclusters via surface motif exchange reaction. *Nat. Commun.* **8**, 1555 (2017).
34. Yao, Q. F. et al. Revealing isoelectronic size conversion dynamics of metal nanoclusters by a noncrystallization approach. *Nat. Commun.* **9**, 1979 (2018).
35. Wu, Z. K. & Jin, R. C. Stability of the two Au-S binding modes in Au₂₅(SG)₁₈ nanoclusters probed by NMR and optical spectroscopy. *ACS Nano* **3**, 2036 (2009).
36. Qian, H. F., Zhu, M. Z., Gayathri, C., Gil, R. R. & Jin, R. C. Chirality in gold nanoclusters probed by NMR spectroscopy. *ACS Nano* **5**, 8935 (2011).
37. Salorinne, K. et al. Conformation and dynamics of the ligand shell of a water-soluble Au₁₀₂ nanoparticle. *Nat. Commun.* **7**, 10401 (2016).
38. Marbella, L. E. & Millstone, J. E. NMR techniques for noble metal nanoparticles. *Chem. Mater.* **27**, 2721 (2015).
39. Badia, A. et al. Gold-sulfur interactions in alkythiol self-assembled monolayers formed on gold nanoparticles studied by solid-state NMR. *J. Am. Chem. Soc.* **119**, 11104 (1997).
40. Parker, J. F., Choi, J. P., Wang, W. & Murray, R. W. Electron self-exchange dynamics of the nanoparticle couple Au₂₅(SC₂Ph)₁₈^(0/1-) by nuclear magnetic resonance line-broadening. *J. Phys. Chem. C*, **112**, 13976 (2008).

Acknowledgements

We acknowledge the financial support from the Ministry of Education, Singapore, Academic Research Grant R-279-000-580-112 and R-279-000-538-114. DFT

computation was supported by the U.S. Department of Energy, Office of Science, Office of Basic Energy Sciences, Chemical Sciences, Geosciences, and Biosciences Division.

Author contributions

J.X. and Y.C. conceived the idea and designed the experiments. J.X. supervised the project. Y.C. carried out the experiments and characterizations. V.F. and D.J. performed the DFT calculations. Y.C., J.X., and D.J. wrote the manuscript. Q.Y., T.C., and S.Z. discussed the results and commented on the manuscript.

Competing interests

The authors declare no competing interests.

Additional information

Supplementary information is available for this paper at <https://doi.org/10.1038/s41467-020-19327-2>.

Correspondence and requests for materials should be addressed to D.-e.J. or J.X.

Peer review information *Nature Communications* thanks Indranath Chakraborty, Hideya Kawasaki and the other, anonymous, reviewer(s) for their contribution to the peer review of this work. Peer reviewer reports are available.

Reprints and permission information is available at <http://www.nature.com/reprints>

Publisher's note Springer Nature remains neutral with regard to jurisdictional claims in published maps and institutional affiliations.



Open Access This article is licensed under a Creative Commons Attribution 4.0 International License, which permits use, sharing, adaptation, distribution and reproduction in any medium or format, as long as you give appropriate credit to the original author(s) and the source, provide a link to the Creative Commons license, and indicate if changes were made. The images or other third party material in this article are included in the article's Creative Commons license, unless indicated otherwise in a credit line to the material. If material is not included in the article's Creative Commons license and your intended use is not permitted by statutory regulation or exceeds the permitted use, you will need to obtain permission directly from the copyright holder. To view a copy of this license, visit <http://creativecommons.org/licenses/by/4.0/>.

© The Author(s) 2020